Incompatibility stresses at grain boundaries in Ni bicrystalline micropillars analyzed by an anisotropic model and slip activity

Idriss Tiba, T. Richeton, Christian Motz, Horst Vehoff, Stéphane Berbenni

Incompatibility stresses at grain boundaries in Ni bicrystalline micropillars analyzed by an anisotropic model and slip activity

I. Tiba,[a,b,*] T. Richeton,[a] C. Motz,[b] H. Vehoff[b] and S. Berbenni[a]

[a] *Laboratoire d'Etude des Microstructures et de Mécanique des Matériaux (LEM3), UMR CNRS 7239, Université de Lorraine, Ile du Saulcy, 57045 Metz, France*

[b] *Chair of Experimental Methods in Materials Science, Saarland University, D-66041 Saarbrücken, Germany*

Abstract—Incompatibility stresses can develop in bicrystals due to material elastic and plastic anisotropies owing to different crystal orientations separated by grain boundaries. Here, these stresses are investigated by combining experimental and theoretical studies on 10 μm diameter Ni bicrystalline micropillars. Throughout stepwise compression tests, slip traces are analyzed by scanning electron microscopy to identify the active slip planes and directions in both crystals. An analytical model is presented accounting for the effects of heterogeneous elasticity coupled to heterogeneous plasticity on the internal mechanical fields. This model provides explicit expressions of stresses in both crystals considering experimentally observed non-equal crystal volume fractions and inclined grain boundaries. It is used to predict the resolved shear stresses on the possible slip systems in each crystal. The predictions of the onset of plasticity as given by the present model in pure elasticity are compared with those given by the classical Schmid's law. In contrast with Schmid's law, the predictions of the analytical model are in full agreement with the experimental observations regarding the most highly stressed crystal and active slip systems. The effects of plastic incompatibilities are also considered in addition to the elastic ones throughout the model. The analysis shows that elastic/plastic coupling incompatibilities together with different crystal volume fractions have significant effects on the slip system activation process.

Keywords: Internal stresses; Anisotropic elasticity; Grain boundaries; Micropillars; Slip-lines

1. Introduction

Many recent studies, both experimental and theoretical, have investigated the mechanical behaviors of single-crystalline micropillars (SCMPs) [1–16] and bicrystalline micropillars (BCMPs) [17–21]. These studies were mainly focused on size effects on the stress–strain response. A "smaller is stronger" hardening effect was associated with a decrease in micropillar diameter [8–12,19]. Spatial–temporal slip intermittency was also studied by analyzing stress and strain drop distributions in SCMPs [11–16].

In the case of BCMPs, incompatible stresses develop in the course of mechanical loading due to grain boundaries (GBs) [22,23]. These incompatibility stresses add to the applied stress and may be responsible for the early initiation of slip bands, which can in turn trigger cracks [24]. Thus, BCMPs are good candidates to compare the theoretical predictions of the activation of slip systems at GBs to the experimental observations. First of all, the amount of slip activity can be predicted by the calculation of elastic and plastic incompatibility stresses which directly affect the resolved shear stress (RSS) values. Second, the slip system activation process may also depend on the dislocation transmission phenomena occurring at GBs [25–29].

A few years ago, important analytical studies [30–32] were carried out to compute the elastic incompatibility stresses in the general context of heterogeneous anisotropic elasticity with small plastic deformations where the bicrystal is composed of two half spaces. This solution was obtained implicitly and was checked by the finite-element method (FEM) regarding stress fields of finite bicrystals to be approximately valid in the neighborhood of GBs [33]. Recently, this solution was retrieved and explicitly derived using field dislocation mechanics theory [34]. It was also observed that analytical explicit solutions perfectly match the FEM results for the same boundary value problem [34]. In the previous approaches, the stress field was considered only for the case where the crystal volume fractions are equal [31,32,34]. To the authors' knowledge, none of these studies considered the full coupling between elastic and plastic incompatibilities with different crystal volume fractions.

In the present paper, the explicit analytical formula will be derived and applied to nickel BCMPs taking into

* Corresponding author at: Laboratoire d'Etude des Microstructures et de Mécanique des Matériaux (LEM3), UMR CNRS 7239, Université de Lorraine, Ile du Saulcy, 57045 Metz, France. Tel.: +33 87 54 73 81; fax: +33 3 87 31 53 66.; e-mail: Idriss.tiba@univ-lorraine.fr

consideration the crystal volume fraction, GB inclination and full anisotropic elasticity/plasticity all together. In Section 2, the mechanical testing of Ni BCMP is introduced. In Section 3, the stress–strain curves and the slip trace analysis are reported. Then, the theory is presented in Section 4. In Section 5, the predictions of the model are discussed in the light of experimental observations and slip transfer parameters.

2. Setup of the Ni BCMPs

2.1. Material preparation

High-purity Ni was investigated (99.99%). Ni has a relatively high elastic anisotropy factor with $A = 2.37\left(A = \frac{2C_{44}}{C_{11}-C_{12}}\right)$. It also presents the advantage of easy observation of slip lines [22,35]. Specimen plates 2 mm thick were heat treated at different temperatures ranging from 1200 to 1400 °C for ~3 days in order to produce a fully recrystallized microstructure with a maximum grain size of 5 mm and GBs more or less normal to the top surface. After each annealing step, the samples were ground, mechanically polished with up to 4000 SiC paper and then finally polished with diamond abrasives down to 0.25 μm. The specimens were then electropolished in order to obtain a perfectly clean surface. Local orientation of the electropolished sample surface was characterized by electron backscattering diffraction (EBSD) performed in a Carl Zeiss ΣIGMA series scanning electron microscope with an acceleration voltage of 20 kV. The angular resolution of the EBSD orientation measurements and the lattice orientation variation within the crystals produces a maximal variation of ±1° in the measurements of the Euler angles. The data processing was performed by Flamenco Channel 5 software (HKL Technology) with an indexing rate of ~99%. The microstructure of the sample was presented by both inverse pole figure (IPF) maps and image quality (IQ) maps.

2.2. Micropillar fabrication processes

The present study focuses only on bicrystals with GBs nearly parallel to the loading direction and with expected high incompatibility stresses. Hence, the numerous Σ3 ⟨1 1 1⟩ twin boundaries (TBs) which developed under the heat treatment [36–39] were not considered since, as reported in Refs. [40,41], no elastic incompatibility stresses develop when TBs are parallel to the loading axis. The chosen crystallographic orientations of both crystals forming the BCMPs are presented in Fig. 1a. These two adjacent grains (CI and CII) have a misorientation angle of 55.1°, which corresponds to a large random angle GB.

Three BCMPs of cylindrical shape were milled along the selected GB using a Strata dual-beam 235 (FEI) focused ion beam (FIB). A 30 kV Ga^+ ion beam was used with a consecutive series of decreasing currents from 20 nA (coarse milling) to 0.05 nA (fine milling). This milling procedure can create slightly tapered BCMPs. The tapering angles for these BCMPs were calculated and were between 2.6° and 3.7°. In addition, the cutting procedure can produce a step at the GB due to different crystallographic orientations of the two grains [42]. The BCMPs have measured diameter at mid-height of ~10 μm and an average height of ~20 μm, which leads to a diameter to length

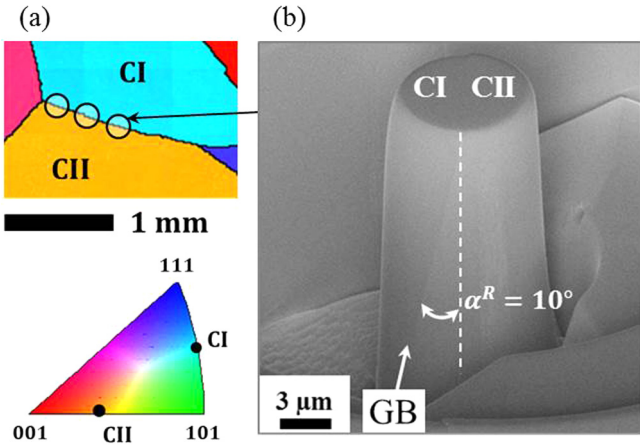

Fig. 1. (a) Inverse pole figure (IPF) map of the local grain structure constituted of two components: crystal I (CI) and crystal II (CII). The crystallographic orientation of each crystal is given in the standard triangle for face-centered cubic materials indicating the normal direction to the map. (b) SEM image of the machined BCMP and GB location after FIB milling.

ratio of ~2. It is worth noting that a variation in the GB plane inclination angle from the loading direction was observed for the three BCMPs: $\alpha^t = 13°$ (BCMP-1), $\alpha^t = 12°$ (BCMP-2) and $\alpha^t = 7°$ (BCMP-3). These values are given without tilt correction. The corrected values are, respectively, $\alpha^R = 10°$, $\alpha^R = 9°$ and $\alpha^R = 4°$ using $\alpha^{R,t} = 90° - \theta^{R,t}$ with a tilt angle of 52° as follows:

$$\theta^R = \tan^{-1}\left(\frac{\tan(\theta^t)}{\sin 52°}\right). \quad (1)$$

Fig. 1b shows a scanning electron microscopy (SEM) image of the BCMP-1 used for compression tests taken from a view at a tilt of 52°.

2.3. Micromechanical testing

Uniaxial compression tests were performed on the three BCMPs by using a flat punch diamond indenter tip with a 20 μm end diameter connected to a Triboindenter (Hysitron) nanoindentation system. The tests were performed in displacement-controlled mode at room temperature with a displacement rate of 1 nm s^{-1}. The tests were interrupted at prescribed strains: 1.5%, 3% and 4.5% for BCMP-1, 1.5%, 3% and 6% for BCMP-2, and 1.5%, 3% and 9% for BCMP-3. Their engineering stress–strain curves were then calculated. The specimens were unloaded at these strains in order to investigate the emerged slip lines. The engineering stress was obtained by dividing the applied load by the BCMP cross-section at mid-height. The engineering strain was calculated as the displacement divided by the initial BCMP average height (~20 μm).

3. Experimental results

The three BCMPs tested showed similar deformation features and therefore, for brevity, only the results from one BCMP (BCMP-1) are presented and analyzed in detail. In the following, BCMP will refer to BCMP-1 for simplicity.

3.1. Stress–strain curves

Fig. 2a displays the stress–strain curve of the BCMP. This curve shows that the specimen started to plastically deform at ~70 MPa. This value is consistent with the one obtained in a previous study with 5 μm diameter Ni BCMPs [19]. As the tests were displacement-controlled, stress drops were observed as in previous works on different metals [14,15,19]. As shown in Fig. 2a, the observed slope of the initial unloading segment (stage no. 1) is approximately the same as in the initial elastic regime. Similarly, the second loading stage is consistent with the preceding unloading stage.

3.2. Slip plane analysis

Fig. 2b shows a representative SEM micrograph of the BCMP after 1.5% strain. This micrograph is taken at a 52° tilt around the normal to the GB trace on the top surface in order to observe the slip lines simultaneously in both crystals. In order to clearly identify the active slip planes, high-magnification images were performed (see Fig. 3) and taken from three different sides of the BCMP. The angle θ^t between the slip lines and the parallel to the top surface was measured directly from the SEM image and corrected for the tilt angle (θ^R) using Eq. (1). In crystal I, single active slip lines with $\theta^R = 49.3°$ are observed (Fig. 3a). The observation of single slip mode is confirmed from another view of the BCMP (Fig. 3c). The corrected angle matches unambiguously the theoretical calculated angle of $50.2 \pm 0.2°$ (assuming variations of $\pm 1°$ in the measurements of the Euler angles) obtained for a D slip plane (see Table 1). At 1.5% strain, the slip lines observed in crystal II belong to two different slip planes, A and B. The planes A and B are clearly visible from the 90° right side of the BCMP (Fig. 3b) where the slip traces have curved shapes. In this case, the angles (θ^t) are measured precisely in the middle of crystal II considering the tangent lines of the slip traces. This procedure yields corrected θ^R values of 43.7° and 28.0°, which match the theoretical calculated angles of $43.0 \pm 2.8°$ and $28.9 \pm 0.3°$ for the A and B slip planes, respectively. Furthermore, faint additional slip traces near the GB were also observed in crystal II at large strains only (3% and 4.5%). The same procedure yields $\theta^R = 68.9°$, which corresponds to the theoretical angle of $68.2 \pm 1.3°$ of slip plane C (see Fig. 4a and b in the next section).

3.3. Slip direction analysis

After identifying the different slip planes in each crystal, information about the slip directions is required to identify the active slip systems. This is possible since slip traces can be observed from different sides. Two coordinate systems are defined (see Fig. 4). The first one (O, x_1, x_2, x_3) corresponds to the frame referred to the BCMP, where x_2 is perpendicular to the GB trace on the top surface and directed from crystal I to crystal II, and x_3 is parallel to the loading direction. The second one (O, x_1^t, x_2^t, x_3^t) corresponds to the tilted position of the BCMP where x_1^t and x_3^t are parallel, respectively, to the horizontal and vertical axes of the SEM image. Fig. 4 shows the BCMP viewed from the GB side, after the second and the third loading stages. From Fig. 4a it can be seen that in crystal II slip clearly occurred on the A and B slip planes and slightly on slip plane C. Fig. 4b gathers three images of the BCMP after the third stage (4.5% strain) at an approximate distance of 1.2 μm from the GB. This figure shows that the slip plane B is observed by forming some shear offsets indicated by the white arrowheads plotted on the right side of the image. This observation is identical to the one in Fig. 5a (viewed from crystal II) with less pronounced shear offsets at 1.5% strain. In addition, it seems that these shear offsets form some kinks with the traces of slip plane A (see Fig. 5b). This means that slip in plane B is out of the plane of observation. Its slip direction coincides with the m^{B4} direction described in the 3-D representation (Fig. 5c). The activation of slip plane A is more clearly characterized by the formation of several discrete shear steps (represented by black arrowheads in Fig. 5a), each carrying a limited shear offset. Their slip direction appears to be parallel to the theoretical m^{A3} slip direction (see the 3-D representation in Fig. 5c). Furthermore, no shear offsets linked to slip plane A are perceptible in the (x_1, x_3) plane (Fig. 5a and slip direction components). That means that the projection of the slip direction vector along x_2 is very low. This observation is fully consistent with the theoretical m^{A3} direction unlike m^{A2} and m^{A6} (see details in Fig. 5). It is noteworthy that the slip direction on plane C cannot be identified since its traces are not clearly visible and only occurred near the GB.

Fig. 6a shows a SEM micrograph of the BCMP after 1.5% strain. Fig. 6b displays a 3-D theoretical

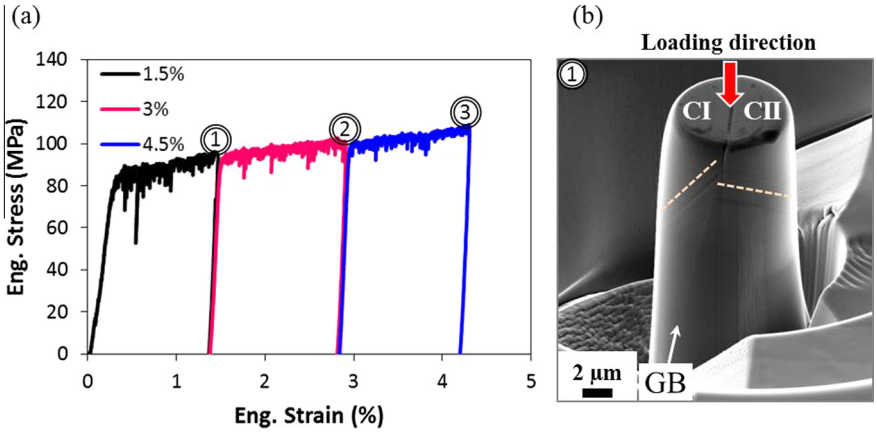

Fig. 2. (a) Typical engineering stress–strain curve of a 10 μm diameter BCMP with three intermediate loading stages. The end of each stage is marked by a number. (b) SEM image of the deformed BCMP taken after the first loading stage, i.e. after 1.5% strain. The loading direction is perpendicular to the BCMP top surface. The dashed lines indicate the emergent slip lines.

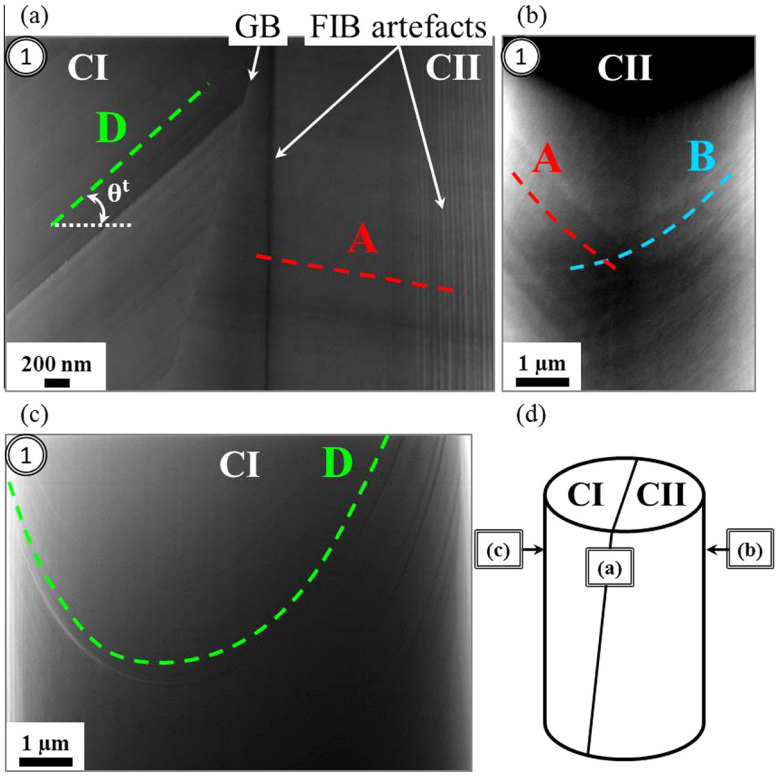

Fig. 3. SEM micrograph of the deformed BCMP after 1.5% strain (loading stage 1) taken from the (a) GB, (b) crystal II and (c) crystal I side views. (d) Schematic representation of the different image views. The crystallographic slip planes are marked with dashed lines and given in Schmid–Boas notation (see Table 1). θ^t is the uncorrected angle between the slip trace line and the parallel to the top surface.

Table 1. Schmid–Boas notation for the 12 conventional $\{1\,1\,1\}$ $\langle 1\,1\,0\rangle$ slip systems of perfect dislocations in face-centered cubic crystals.

n^s	m^s	Schmid–Boas	n^s	m^s	Schmid-Boas
$(1\,1\,1)$	$[0\,\bar{1}\,1]$	B2	$(\bar{1}\,1\,1)$	$[0\,\bar{1}\,1]$	A2
$(1\,1\,1)$	$[1\,0\,\bar{1}]$	B4	$(\bar{1}\,1\,1)$	$[\bar{1}\,0\,\bar{1}]$	A3
$(1\,1\,1)$	$[\bar{1}\,1\,0]$	B5	$(\bar{1}\,1\,1)$	$[1\,1\,0]$	A6
$(1\,\bar{1}\,1)$	$[0\,\bar{1}\,\bar{1}]$	D1	$(1\,1\,\bar{1})$	$[0\,\bar{1}\,\bar{1}]$	C1
$(1\,\bar{1}\,1)$	$[\bar{1}\,0\,1]$	D4	$(1\,1\,\bar{1})$	$[\bar{1}\,1\,0]$	C5
$(1\,\bar{1}\,1)$	$[1\,1\,0]$	D6	$(1\,1\,\bar{1})$	$[1\,0\,1]$	C3

representation of the BCMP tilted at 52° and viewed from crystal I. The slip plane D and the three slip directions m^{D1}, m^{D4} and m^{D6} are plotted. It can be seen that the observed slip trace shapes (Fig. 6a) are consistent with the theoretical ones (Fig. 6b). Differences in contrast show the emergence of slip traces represented by white arrowheads in Fig. 6a. These shear offsets are heavily emitted along one major direction, which appears in the same direction as the theoretical m^{D6} slip direction (Fig. 6b). In addition, the shear offsets almost disappear in the (x_1, x_3) plane (Fig. 6a), meaning that the projection of the slip direction along x_2 is low. Among the three directions associated with the D plane, m^{D6} exhibits the lowest x_2 component (see Fig. 6).

It is important to note that the same slip systems were identified in the two other BCMPs.

4. Analytical model

4.1. Notations and problem definition

In the following equations, the contracted Voigt notation [43] is adopted: 11 → 1, 22 → 2, 33 → 3, 23 → 4, 13 → 5 and 12 → 6, and for consistency, an engineering convention is considered for strain components, i.e. $\varepsilon_4 = 2\varepsilon_{23}$, $\varepsilon_5 = 2\varepsilon_{31}$ and $\varepsilon_6 = 2\varepsilon_{12}$. The subscripts i and j will be used for reduction notation with $i,j = 1,\ldots,6$. The subscripts p and q will be used for vector notation with $p,q = 1,\ldots,3$.

An infinite bicrystal with planar GB subjected to macroscopic homogeneous stress Σ_i and undergoing piecewise uniform plastic strains ε_i^P is considered. The bicrystal configuration is displayed in Fig. 7 considering two different assumptions regarding elasticity: heterogeneous anisotropic elasticity (Fig. 7a) and homogeneous isotropic elasticity (Fig. 7b).The superscript I is used for fields referring to crystal I and II for fields in crystal II. The jump or difference of a mechanical field or material property d at the interface is denoted $[d] = d^{II} - d^{I}$. f is the volume fraction of crystal I in the infinite medium. Thus, $1 - f$ is the volume fraction of crystal II. The infinite GB plane spreads in the $\left(O,\ x_1^{GB},\ x_3^{GB}\right)$ plane with unit normal $\left(n_q^{GB}\right)$ directed toward crystal II from crystal I.

4.2. Incompatibility stresses

Following Ref. [34], the present model derives explicit expressions for the stress fields in the general case of

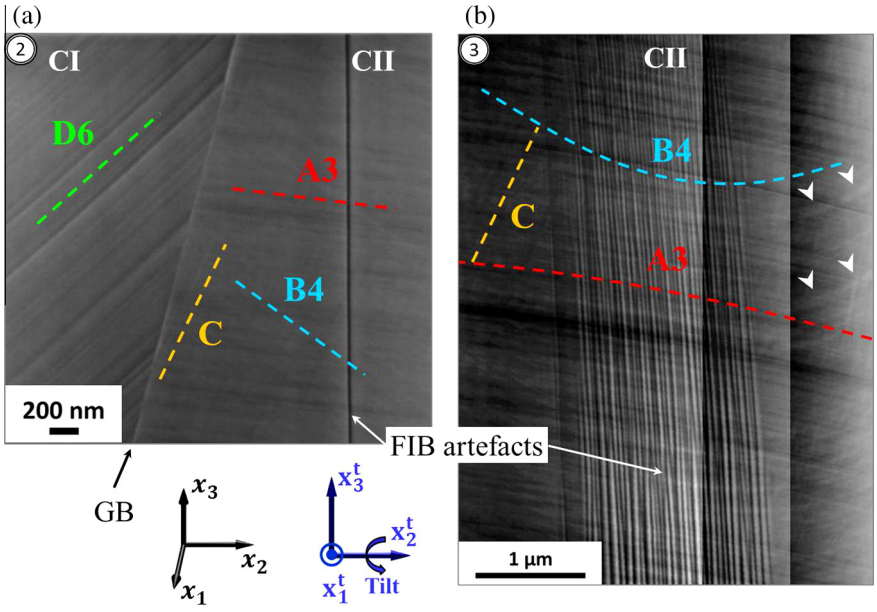

Fig. 4. SEM micrograph of the same BCMP as in Fig. 3 taken after (a) the second (3% straining) and (b) the third (4.5% straining) loading stages (Fig. 2) from the GB side view. The slip planes, A, B and C are indicated with dashed lines. Arrowheads indicate the shear offsets produced by the B slip plane motion.

heterogeneous anisotropic elasticity coupled with heterogeneous plasticity. In addition, the case of non-equal crystal volume fractions is incorporated in the present paper. These formulae were obtained by solving the field equations of static field dislocation mechanics theory [44].

4.2.1. General case: heterogeneous anisotropic elasticity with plastic incompatibilities

In the general case of piecewise uniform anisotropic elasticity and averaged (or uniform) plastic strains with non-zero macroscopic stress and non-equal volume fraction f, the stress tensors are uniform in crystals I and II and can be explicitly written as follows:

$$\begin{aligned}
\sigma_1^I &= \Sigma_1 - (1-f)\left(G_{11}\left[\varepsilon_1^*\right] + G_{13}\left[\varepsilon_3^*\right] + G_{15}\left[\varepsilon_5^*\right]\right)\\
\sigma_2^I &= \Sigma_2\\
\sigma_3^I &= \Sigma_3 - (1-f)\left(G_{13}\left[\varepsilon_1^*\right] + G_{33}\left[\varepsilon_3^*\right] + G_{35}\left[\varepsilon_5^*\right]\right)\\
\sigma_4^I &= \Sigma_4\\
\sigma_5^I &= \Sigma_5 - (1-f)\left(G_{15}\left[\varepsilon_1^*\right] + G_{35}\left[\varepsilon_3^*\right] + G_{55}\left[\varepsilon_5^*\right]\right)\\
\sigma_6^I &= \Sigma_6
\end{aligned} \tag{2}$$

$$\begin{aligned}
\sigma_1^{II} &= \Sigma_1 + f\left(G_{11}\left[\varepsilon_1^*\right] + G_{13}\left[\varepsilon_3^*\right] + G_{15}\left[\varepsilon_5^*\right]\right)\\
\sigma_2^{II} &= \Sigma_2\\
\sigma_3^{II} &= \Sigma_3 + f\left(G_{13}\left[\varepsilon_1^*\right] + G_{33}\left[\varepsilon_3^*\right] + G_{35}\left[\varepsilon_5^*\right]\right)\\
\sigma_4^{II} &= \Sigma_4\\
\sigma_5^{II} &= \Sigma_5 + f\left(G_{15}\left[\varepsilon_1^*\right] + G_{35}\left[\varepsilon_3^*\right] + G_{55}\left[\varepsilon_5^*\right]\right)\\
\sigma_6^{II} &= \Sigma_6
\end{aligned} \tag{3}$$

where $\left[\varepsilon_i^*\right] = [s_{ij}]\Sigma_j + [\varepsilon_i^p]$, s_{ij} are the elastic compliances that include the multiplying factors of 2 and 4 [43], and the G_{ij} symmetric matrix non-zero components in Eqs. (2) and (3) are given by:

$$\begin{aligned}
G_{11} &= (\tilde{s}_{33}\tilde{s}_{55} - \tilde{s}_{35}^2)/D, \quad G_{13} = (\tilde{s}_{15}\tilde{s}_{35} - \tilde{s}_{13}\tilde{s}_{55})/D\\
G_{33} &= (\tilde{s}_{11}\tilde{s}_{55} - \tilde{s}_{15}^2)/D, \quad G_{15} = (\tilde{s}_{13}\tilde{s}_{35} - \tilde{s}_{15}\tilde{s}_{33})/D\\
G_{55} &= (\tilde{s}_{11}\tilde{s}_{33} - \tilde{s}_{13}^2)/D, \quad G_{35} = (\tilde{s}_{13}\tilde{s}_{15} - \tilde{s}_{35}\tilde{s}_{11})/D
\end{aligned} \tag{4}$$

with $\tilde{s}_{ij} = (1-f)s_{ij}^I + fs_{ij}^{II}$ and

$$D = \tilde{s}_{11}\tilde{s}_{35}^2 + \tilde{s}_{33}\tilde{s}_{15}^2 + \tilde{s}_{55}\tilde{s}_{13}^2 - \tilde{s}_{11}\tilde{s}_{33}\tilde{s}_{55} - 2\tilde{s}_{13}\tilde{s}_{15}\tilde{s}_{35} \tag{5}$$

The above explicit solutions show coupled effects of elastic and plastic incompatibilities at the interface. These expressions represent extensions of explicit formulas derived in Ref. [34] for non-equal crystal volume fractions to derive the long-range stress fields in both crystals.

It should be mentioned that two other stress contributions are disregarded in the present model and are left for future studies: (i) stress contributions due to the presence of free surfaces which are here rejected at infinity (in contrast with FEM simulations [33]); and (ii) stress contributions due to the discreteness of slip interacting with GB [35,45,46] and dislocation pile-ups [26,47].

4.2.2. Homogeneous isotropic elasticity with plastic incompatibilities

In the case of homogeneous isotropic elasticity characterized by uniform Young's modulus E and uniform Poisson's ratio ν through the bicrystal (hence the shear modulus is obtained by $\mu = \frac{E}{2(1+\nu)}$) (Fig. 7b), Eqs. (2)–(5) simplify to:

$$\begin{aligned}
\sigma_1^I &= \Sigma_1 + \frac{2\mu}{1-\nu}(1-f)([\varepsilon_1^p] + \nu[\varepsilon_3^p])\\
\sigma_2^I &= \Sigma_2\\
\sigma_3^I &= \Sigma_3 + \frac{2\mu}{1-\nu}(1-f)([\varepsilon_3^p] + \nu[\varepsilon_1^p])\\
\sigma_4^I &= \Sigma_4\\
\sigma_5^I &= \Sigma_5 + \mu(1-f)[\varepsilon_5^p]\\
\sigma_6^I &= \Sigma_6
\end{aligned} \tag{6}$$

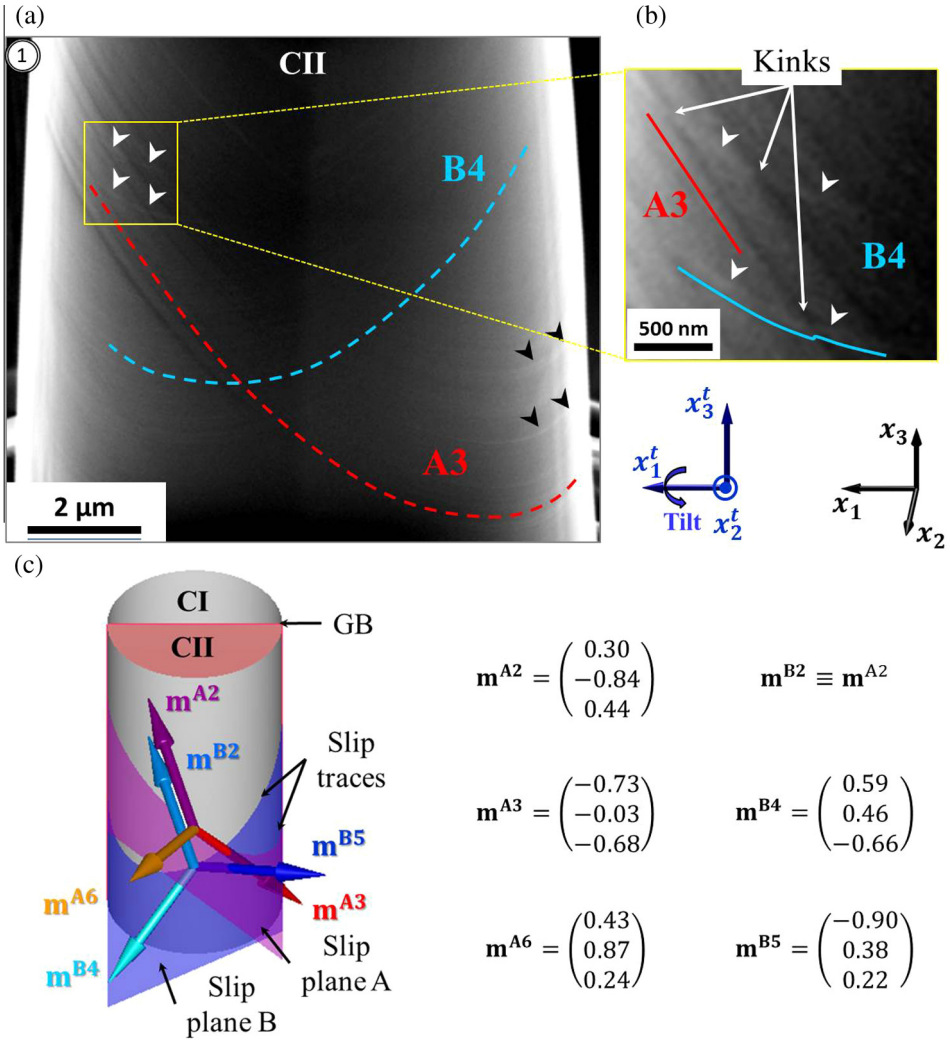

Fig. 5. (a) BCMP SEM micrograph taken after 1.5% straining (loading cycle no. 1) from the crystal II side. The slip planes A and B are indicated with dashed lines. Shear offsets on slip planes A and B are indicated with black and white arrowheads, respectively. (b) Closer view of some kinks formed between the B4 and A3 slip systems seen in (a). (c) BCMP 3-D theoretical representation showing the slip plane traces, A and B, and their possible slip directions, m^{A2}, m^{A3}, m^{A6}, m^{B2}, m^{B4} and m^{B5}. All the theoretical slip direction components are expressed in the frame (O, x_1, x_2, x_3).

$$
\begin{aligned}
\sigma_1^{II} &= \Sigma_1 - \frac{2\mu}{1-\nu} f([\varepsilon_1^p] + \nu[\varepsilon_3^p]) \\
\sigma_2^{II} &= \Sigma_2 \\
\sigma_3^{II} &= \Sigma_3 - \frac{2\mu}{1-\nu} f([\varepsilon_3^p] + \nu[\varepsilon_1^p]) \\
\sigma_4^{II} &= \Sigma_4 \\
\sigma_5^{II} &= \Sigma_5 - \mu f[\varepsilon_5^p] \\
\sigma_6^{II} &= \Sigma_6
\end{aligned}
\tag{7}
$$

It is noteworthy that these isotropic elasticity solutions were previously obtained by other techniques in [48,49].

4.2.3. Schmid's law

In the case where the classic Schmid's law is used, the stress tensor in each component crystal is equal to the macroscopic stress:

$$\sigma_i^I = \sigma_i^{II} = \Sigma_i \tag{8}$$

which means that both crystals are uniformly stressed. In contrast, Eqs. (2) and (3) contain both the applied stress and the incompatibility stresses. Note that the uniform stress assumption (Eq. (8)) represents a particular case of the present one when homogeneous elasticity and plasticity are considered in Eqs. (2) and (3) (i.e. $[\varepsilon_i^*] = [s_{ij}]\Sigma_j + [\varepsilon_i^p] = 0$).

4.3. Resolved shear stress and plastic strain

In order to compare the predictions of the theoretical approach with the experimental results analyzed in Section 3, the resolved shear stress (RSS), τ^s, on a given slip system s in a given crystal (I or II) is obtained from:

$$\tau^s = R_i^s \sigma_i \tag{9}$$

where σ_i are calculated using Eqs. (2) and (3), and R_i^s is the classic Schmid's orientation tensor using the same reduction convention as before (i.e. $R_4 = 2R_{12}$, $R_5 = 2R_{31}$, $R_6 = 2R_{23}$) together with:

$$R_{pq}^s = \frac{1}{2}\left(m_p^s n_q^s + n_p^s m_q^s\right) \tag{10}$$

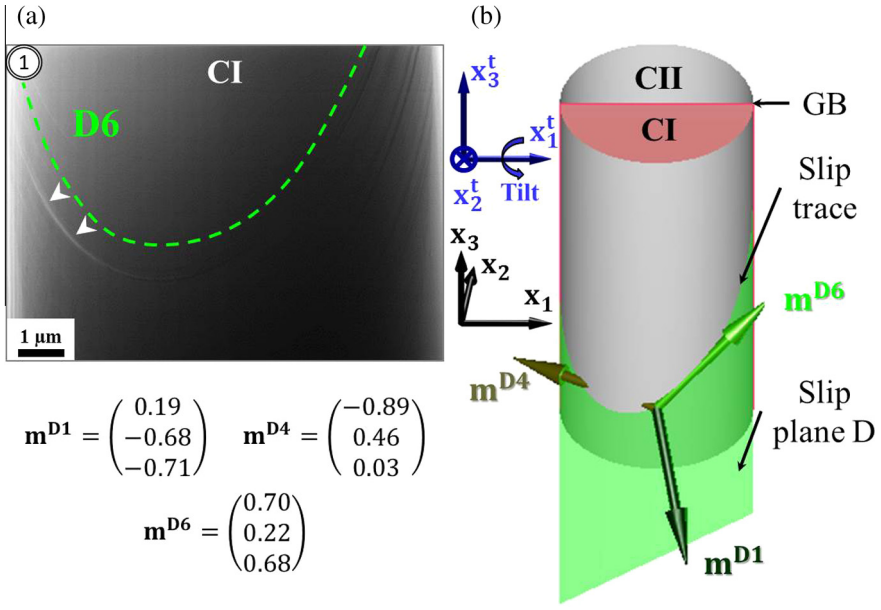

Fig. 6. (a) SEM micrograph (reproduced from Fig. 3c). Arrowheads indicate the shear offsets. (b) 3-D theoretical representation of the BCMP tilted at 52° showing the theoretical slip plane D emergence at the crystal I lateral surface with the three possible directions: m^{D1}, m^{D4} and m^{D6}. The theoretical components of m^{D1}, m^{D4} and m^{D6} are expressed in the frame (O, x_1, x_2, x_3).

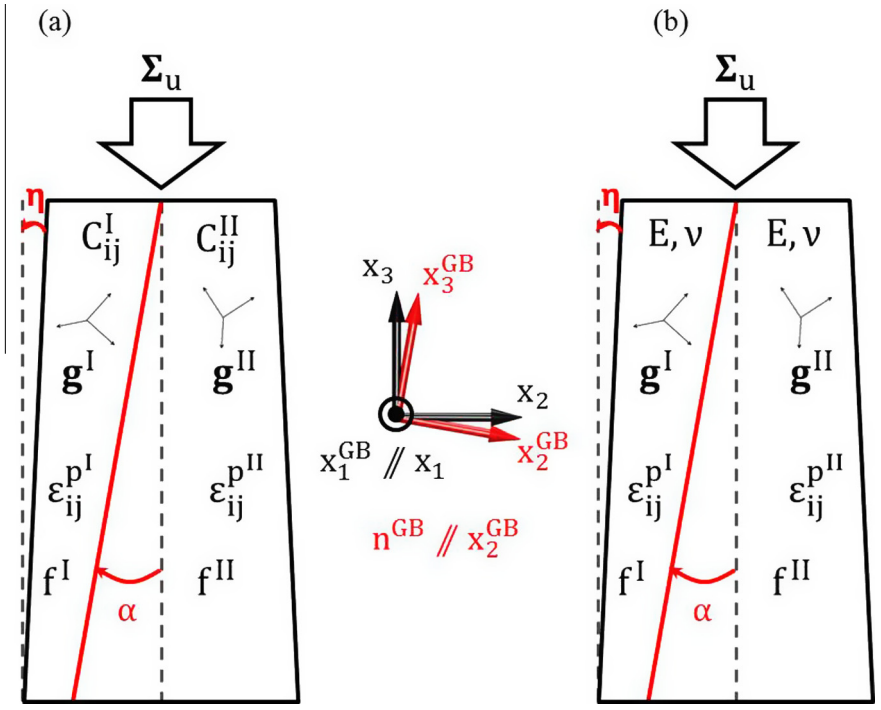

Fig. 7. Schematic layout of the BCMP studied in Section 3. The GB plane spreads in the $(O,\ x_1^{GB},\ x_3^{GB})$ plane with normal n_q^{GB} directed from crystal I to crystal II. The x_1 direction points out of the image. The angle α and η define, respectively, the GB inclination and the tapering angles from the loading axis. $\mathbf{g}^I$ ($\mathbf{g}^{II}$) and f^I (f^{II}) are the crystallographic orientations and the volume fractions of crystal I (crystal II), respectively. $\varepsilon_i^{p^I}$ and $\varepsilon_i^{p^{II}}$ are the uniform piecewise plastic strain in crystal I and crystal II, respectively. (a) General case of heterogeneous anisotropic elasticity with plastic incompatibilities. C_{ij}^I and C_{ij}^{II} are the respective elastic stiffness tensors in reduction notation. (b) Case of homogeneous isotropic elasticity with plastic incompatibilities.

where m_p^s is the unit vector in the slip direction and n_p^s is the unit vector normal to the slip plane (see Table 1). The plastic strain tensor ε_i^p for a given crystal (I or II) is given by:

$$\varepsilon_i^p = \sum_s \gamma^s R_i^s \tag{11}$$

where γ^s are the slip magnitudes of slip systems. For a given slip increment $\Delta\gamma^s$, the plastic work increment ΔW^p in a given crystal should be positive according to the second law of thermodynamics and is defined by:

$$\Delta W^p = \sum_s \tau^s \Delta\gamma^s \geqslant 0 \tag{12}$$

4.4. Calculation method

A numerical code based on the software package Matlab (R2009b) was developed to compute the RSSs in both crystals from Eqs. (2)–(11). The input parameters for simulating slip activity are the crystallographic orientations represented by the Euler angle triplet (φ_1, ϕ, φ_2) measured by EBSD before the loading procedure, the 12 slip systems presented in Table 1 and the three elastic constants for Ni. The elastic constants were taken from Ref. [50] and are listed in Table 2. All the parameters defining the RSSs should be expressed in the same coordinate frame, which was selected as the GB plane coordinate system, $\left(O,\ x_1^{GB},\ x_2^{GB},\ x_3^{GB}\right)$ with x_2^{GB} normal to the GB plane and $x_1^{GB} \equiv x_1$ (see Fig. 7). The elastic compliances tensors and the Schmid orientation tensors are thus rotated twice, first from the crystal frame to the global frame according to the values of the Euler angles, then from the global frame to the GB frame.

5. Predictions of the model and discussion

5.1. Slip prediction in the case of pure elasticity

The expressions of the stress components are now applied to the specific geometry of the BCMP analyzed in Section 3. In this first step, no plastic strain is considered in order to study slip activity at the onset of plastic deformation (i.e. at the stress state corresponding to the yield point in Fig. 2). The experimental GB inclination angle $\alpha = \alpha^R = -10°$ and the volume fraction are taken into consideration in the calculations. The volume fraction is computed by considering α and the tapering angle of this BCMP, $\eta = \eta^R = 3.7°$ (Fig. 7). Hence, the obtained volume fraction of crystal I is $f = 0.25$. In order to study the specific effects of the crystal volume fraction and the GB inclination angle, three additional cases are also considered: (i) $f = 0.5$ and $\alpha = 0°$, (ii) $f = 0.5$ and $\alpha = -10°$, and (iii) $f = 0.25$ and $\alpha = 0°$.

Following the different assumptions mentioned above, Table 3 shows the three and six highest ranked RSSs, normalized by the uniaxial applied (macroscopic) stress Σ_u, for crystal I and crystal II, respectively. These values are computed from Schmid's law and from the model described in Section 4. A maximum error bar of ± 0.01 was obtained on these values, assuming possible variations of $\pm 1°$ in the measurements of the Euler angles. It is worth noting that significantly lower errors are actually obtained for the normalized RSSs on the observed slip systems. Accordingly, large differences were found between the RSS values given by the two methods, well beyond the scope of possible error of measurements. Indeed, the highest RSS is predicted to be the D6 slip system in crystal I by the present model, whereas the highest RSS is predicted to be either the A3 or the B4 slip system in crystal II with a certain ambiguity using Schmid's law. Thus, a detailed analysis is now proposed with new parameters to quantify in depth both the onset of plasticity and the slip system mode in the light of the previous experimental analysis.

5.1.1. Onset of plasticity

The first important feature of the bicrystal's mechanical behavior is knowledge of where slip occurs. In particular, the question is to determine in which component slip is first activated. For that, the difference between the maximum RSS in crystal I $\left(\tau^I_{max}\right)$ and the maximum RSS in crystal II $\left(\tau^{II}_{max}\right)$ normalized by the magnitude of the uniaxial macroscopic stress Σ_u is considered:

$$R_1 = \frac{\tau^I_{max} - \tau^{II}_{max}}{|\Sigma_u|} \tag{13}$$

The values of this parameter are displayed in Table 4. It can be seen that both the sign and the magnitude of R_1 are different between Schmid's law ($R_1 = -0.07$) and the present model ($R_1 = +0.21$ considering the real BCMP geometry). According to Schmid's law, plasticity would start in crystal II with relatively low difference with crystal I, whereas according to the present model, plasticity would start in crystal I with a large difference with crystal II. These last predictions are confirmed by the experimental observations reported on Figs. 3 and 6 and analyzed in Section 3, thus demonstrating the relevance of the present model to describe the onset of plasticity. In the picture of Fig. 3a, which is taken at high magnification after a macroscopic strain of 1.5%, it can indeed been confirmed that the slip bands are very much more pronounced in crystal I than in crystal II. Moreover, Table 4 shows also that, here, both the GB inclination and the crystal volume fraction have little influence on R_1. Nevertheless, the different volume fraction of crystal I with respect to crystal II appears to influence the results more than the GB inclination.

5.1.2. Active slip systems and slip modes

The predictions of the present model are now analyzed in terms of the ranking of active slip systems and are compared to Schmid's law. According to Schmid's law, the first three systems with highest RSS values in crystal I are, in decreasing order, D1, D6 and B2, whereas the present model yields D6, D1 and B2 (see Table 3). By varying the crystal volume fraction and the GB inclination in the model, the ranking of slip systems remains the same. However, the variation of the volume fraction has an impact on the RSS values. In the real BCMP configuration ($f = 0.25$ and $\alpha = -10°$), more significant differences regarding the normalized RSSs were clearly observed from Table 3 between the model and Schmid's law in crystal I ($\sim$0.22) compared to the model case with equal volume fractions ($\sim$0.12). Indeed, from Eqs. (2) and (3), the magnitude of the incompatibility stresses in one crystal is roughly proportional to the volume fraction of the other crystal. Hence,

Table 2. Elastic stiffness values and isotropic elastic constants for Ni used in the calculations. The anisotropy factor is represented by A $\left(A = \frac{2C_{44}}{C_{11}+C_{12}}\right)$.

C_{11} (GPa)	C_{12} (GPa)	C_{44} (GPa)	A	ν	μ (GPa)
244	158	102	2.37	0.31	78.4

Table 3. The three (six) maximum RSS values normalized by the macroscopic uniaxial loading stress $|\tau^s/\Sigma_u|$ as predicted by the two models in crystal I (crystal II). Highest values are written in bold. The present model was applied in the elastic regime. The normalized RSS values are obtained with a maximal error of ± 0.01, considering variations of $\pm 1°$ in the measurements of the Euler angles. For the observed slip systems, much lower errors are actually obtained.

Slip system	$\lvert\tau^s/\sum_u\rvert$				
	Present model				Schmid
	$f=0.5$ $\alpha^R=0°$	$f=0.5$ $\alpha^R=-10°$	$f=0.25$ $\alpha^R=0°$	$f=0.25$ $\alpha^R=-10°$	
Crystal I					
D6	**0.53**	**0.54**	**0.62**	**0.63**	**0.41**
D1	0.47	0.47	0.52	0.52	**0.42**
B2	0.28	0.31	0.33	0.37	0.26
Crystal II					
B4	**0.37**	**0.37**	**0.42**	**0.42**	**0.49**
A3	0.32	0.33	0.39	**0.40**	**0.49**
B2	0.27	0.26	0.29	0.29	0.33
C1	0.29	0.27	0.30	0.28	0.32
D1	0.22	0.22	0.27	0.27	0.33
A2	0.24	0.23	0.27	0.27	0.32

Table 4. R_1-values in crystals I and II obtained from Schmid's law and the present model. Variations of $\pm 1°$ in the measured Euler angles induce errors of the order of ± 0.01 in the R_1-values.

Present model				Schmid
$f=0.5$ $\alpha=0°$	$f=0.5$ $\alpha=-10°$	$f=0.25$ $\alpha=0°$	$f=0.25$ $\alpha=-10°$	
0.16	0.17	0.20	0.21	−0.07

contrary to crystal II, the model predictions differ significantly from Schmid's law in crystal I due to a strong effect of volume fraction on incompatibility stresses. For instance, the real situation ($f=0.25$ and $\alpha=-10°$) promotes the predominance of the activated D6 slip system in crystal I with the highest normalized RSS value in Table 3, i.e. $|\tau^s/\Sigma_u|=0.63$. Furthermore, the ratio R_2 between the highest RSS and the second highest RSS in a crystal can be introduced to predict the slip mode, i.e. single slip or double (or multiple) slip:

$$R_2=\frac{\tau_{max1}}{\tau_{max2}}. \tag{14}$$

A ratio R_2 near to unity indicates that plasticity should begin with double or multiple slip, whereas a high R_2 value is expected to characterize single slip. Table 5 reports the different values of R_2 and shows a strong discrepancy in crystal I between Schmid's law and the present model. Double slip on coplanar systems D1 and D6 is expected from Schmid's law from $R_2=1.04$. On the contrary, single slip on the D6 system is expected from the present model from $R_2=1.22$ when considering the real BCMP geometry. Thus, the present model's prediction is in full agreement with the active slip plane and slip direction analyzed as the D6 system experimentally in Section 3. From Table 5, it is also interesting to note the important physical effect of crystal volume fraction on R_2 in crystal I which increases from 1.13 for $f=0.5$ (representing a fictive model case) to 1.22 for $f=0.25$ (representing the real case). The latter is in better agreement with observed slip activity. The influence of the GB inclination on R_2 is much weaker than the crystal volume fraction effect.

A similar analysis shows that there is less difference between Schmid's law and the proposed model in crystal II. Both approaches predict double slip on systems A3 and B4 with $R_2=1.01$ from the Schmid's law and $R_2=1.05$ from the model (see Tables 3 and 5). These predictions are completely consistent with the analyses of Sections 3.2 and 3.3 where the activation of the A3 and B4 systems in crystal II even at low strain were reported (see Fig. 3b).

5.2. Slip prediction in the case of elastic anisotropy with plastic incompatibilities

Both the experimental observations and the consideration of incompatibility stresses due to heterogeneous elasticity suggest that crystal I first undergoes a single slip mode

Table 5. R_2-values in crystals I and II obtained from Schmid's law and the present model. Variations of $\pm 1°$ in the measured Euler angles induce a maximum error of ± 0.02 in the R_2-values.

Crystal	Present model				Schmid
	$f=0.5$ $\alpha=0°$	$f=0.5$ $\alpha=-10°$	$f=0.25$ $\alpha=0°$	$f=0.25$ $\alpha=-10°$	
I	1.13	1.13	1.20	1.22	1.04
II	1.15	1.12	1.07	1.05	1.01

on the D6 system. As a consequence, the predictions of active slip systems in crystal II may be refined with the present model considering the effect of primary single slip on the D6 system in crystal I. Hence, the RSS values in crystal II are computed using Eqs. (3)–(5) together with Eqs. (9) and (10), still considering no plastic strain in crystal II, but now adding plastic strain in crystal I due to single slip on the D6 system. From Eq. (11), the plastic strain increment $\Delta\varepsilon_i^{p^I}$ can be written:

$$\Delta\varepsilon_i^{p^I} = \left(\Delta\gamma^{D6} R_i^{D6}\right)^I \tag{15}$$

where $\Delta\gamma^{D6^I}$ is such that $(\tau^{D6}\Delta\gamma^{D6})^I \geqslant 0$ according to Eq. (12). In Eq. (15) and in the following discussion, only the average slip in crystal I is considered. Nevertheless, this assumption remains consistent with the roughly homogeneously distributed slip traces within this crystal as observed in Fig. 4.

Consequently, the RSS values in both crystals now depend on both Σ_u and $\Delta\gamma^{D6^I}$ according to Eqs. (2)–(5). Thus, for consistency, a realistic value of Σ_u must be taken in the calculation in order to consider realistic values of $\Delta\gamma^{D6^I}$. From the linear regime of the experimental stress–strain curve (Fig. 2a), it is assumed that $\Sigma_u = -70$ MPa at the onset of plasticity. For comparison, the RSS values are also computed from the homogeneous isotropic elasticity model (Eqs. (6) and (7)) with the same assumptions about plastic strain. Fig. 8 displays the theoretical normalized RSS values on systems A3 and B4 in crystal II as functions of the slip magnitude on system D6 in crystal I. The isotropic elastic constants used in the calculation are deduced from the anisotropic ones by using the Voigt average assumption [51] (see Table 2). Fig. 8 exhibits a linear increase of the RSS values with $\Delta\gamma^{D6^I}$ for both approaches. For the present model, a switch between systems B4 and A3 is observed: for $\gamma^{D6^I} \sim 0.073\%$, the RSS value on slip system A3 becomes higher than that on slip system B4 (see Fig. 8). When this transition occurs, the RSS values of both slip systems A3 and B4 are approximately $0.52|\Sigma_u|$. This value is smaller than that of the D6 system in crystal I ($0.63|\Sigma_u|$, see Table 3). This suggests that the switch between the B4 and A3 RSS values probably occurs before the onset of plasticity in crystal II. Afterwards, both approaches predict a slight prominence of the A3 system without necessarily invalidating the double-slip mode conjecture. The initial prominence of the A3 system can be experimentally confirmed according to Fig. 3a where only slip bands

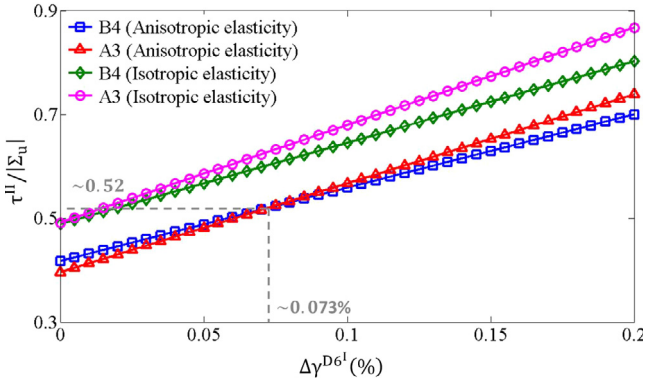

Fig. 8. Variation of RSS values on systems A3 and B4 in crystal II as a function of slip magnitude on the D6 system in crystal I. Comparisons between anisotropic and isotropic cases.

corresponding to the A3 system are observed near the GB after 1.5% macroscopic strain.

5.3. Comparisons with GB slip transfer geometrical parameters

The observations and the calculations indicate that plasticity starts in crystal I in the D6 system and is first followed by the activation of A3 system in crystal II. This scenario suggests that plastic deformation may be transmitted at the GB from slip system D6 in crystal I to slip system A3 in crystal II. In order to establish a connection between the present model and the GB slip transmission process, some geometrical parameters commonly used in the literature [25–28] are now determined. First of all, the conventional slip transfer parameter at GB, denoted M and defined by Shen et al. [27] as:

$$M = \left(L_p^I L_p^{II}\right)\left(m_p^I m_p^{II}\right) \tag{16}$$

is considered. Here, L_p^I and L_p^{II} are the unit vectors of intersection lines made by the incoming and the outgoing slip planes with the GB, and m_p^I and m_p^{II} are slip directions unit vectors of these planes. Shen et al. [27] concluded that slip transfer will be favored in the case of the highest M-value, so that the angles between (i) L_p^I and L_p^{II} and (ii) m_p^I and m_p^{II} are minimized. Lee et al. [26] and Lim and Raj [29] proposed one additional condition to take into account the effect of dislocation pile-up formation in the incoming slip system on the RSS on the outgoing slip system. This condition is based on the minimization of the residual Burgers vector magnitude $|b_r|$ left at the GB.

The intersection angles at the GB between the incoming (in crystal I) and the outgoing (in crystal II) slip planes, $\delta = arccos\left(L_p^I L_p^{II}\right)$, and between slip directions, $\lambda = arccos\left(m_p^I m_p^{II}\right)$, as well as the M-values and $|b_r|$ are listed in Table 6. In Table 6, $|b_r|$ is normalized with the Burgers vector magnitude b for perfect lattice dislocations in Ni. It is shown that the minimum angle condition on δ occurs between the incoming slip plane D and the outgoing slip plane C with $\delta = 4°$. In addition, among the possible directions lying on this slip plane, the highest geometric factor with $M = 0.98$ and the lowest residual Burgers vector with $|b_r|/b = 0.19$ both correspond to the C3 system (see

Table 6. Intersection angles at the GB between incoming and outgoing slip planes (δ), slip directions (λ), M-values and the $|b_r|/b$ normalized residual Burgers vector. b is the magnitude of the Burgers vector for Ni. These values are computed from the initial Euler angles of both crystals. The errors bars on the angles δ and λ are about $\pm 1°$.

Crystal I	Crystal II	δ (°)	λ (°)	M	$\lvert b_r\rvert/b$
D6	B2		71	0.17	1.16
	B4	59	86	0.03	1.37
	B5		67	0.20	1.10
	D1		54	0.03	0.91
	D4	87	86	0.00	1.37
	D6		49	0.04	0.83
	A2		71	0.31	1.16
	A3	18	11	0.93	0.19
	A6		49	0.62	0.83
	C1		54	0.58	0.91
	C5	4	67	0.40	1.10
	C3		11	0.98	0.19

Table 6). From experimental observations, the slip plane C effectively occurred slightly but only at large strains and near the GB. Moreover, the slip direction on this plane could not be experimentally identified (see Fig. 4). Table 6 points out that system A3 has also very favorable transmission parameters with $M = 0.93$ and $|b_r|/b = 0.19$, whereas system B4 has very poor transmission parameters ($M = 0.03$ and $|b_r|/b = 1.37$). Hence, our observations of slip activity in crystal II can be summed up as follows:

- system A3, clearly observed at low strains and predominant near the GB, has both favorable transmission parameters and high RSS considering elastic and plastic incompatibilities with crystal I;
- system B4, observed at low strains, has high RSS considering incompatibilities with crystal I but very poor transmission parameters;
- system C3, slightly observed at large strains and near the GB only, has favorable transmission parameters but low RSS.

For this BCMP, incompatibility stresses are hence of primary importance for the prediction of the main slip systems. Thus, the present model may be considered as a new basic tool, complementary to slip transfer criteria, for predicting favorable active slip systems in BCMPs.

6. Conclusions

In the present paper, a slip line analysis near planar GBs in Ni BCMPs, 10 μm in diameter and with an aspect ratio of ~2, was investigated by means of stepwise microcompression tests using a flat punch nanoindenter. Experimental results were compared to a theoretical formulation designed for the prediction of incompatibility stresses and RSS values in both crystals. The explicit expressions of stresses in each crystal were obtained in the general context of heterogeneous and anisotropic elasticity with plastic incompatibilities. In addition to the crystallographic orientations, this model accounts for elastic anisotropy and the BCMP geometry through the crystal volume fractions and GB inclination angle. The proposed model was used to predict the RSS values in both crystals. The results were given in detail for the BCMP that exhibits the largest GB inclination angle. The same conclusions apply to the two other BCMPs. All the predictions were consistent with the experimental slip analysis. In contrast, Schmid's law considers only and independently the crystallographic orientation of each crystal and clearly failed to predict the onset of plasticity and D6 single-slip activation in crystal I. Here, a strong influence of elastic anisotropy on slip predictions was observed although the elastic anisotropy of Ni ($A = 2.37$) is relatively moderate compared to other materials, e.g. Cu ($A = 3.26$). Significant effects of crystal volume fraction and plasticity in the neighboring crystal were also reported. However, a limited contribution of the GB inclination was observed. The good agreement between theory and experiment indicates that incompatibility stresses play a key role in slip activation in BCMPs constituted of elastic anisotropic crystals and may have a significant impact on slip transfer models.

Acknowledgements

The authors are grateful to the French Ministry of Higher Education and Scientific Research and the French-German University (UFA-DFH) for financial supports. T.R. is grateful to the French National Research Agency (ANR) for financial support under contract "PHIRCILE" (ANR 2010 JCJC 0914 01).

References

[1] M.D. Uchic, D.M. Dimiduk, Mater. Sci. Eng. A 400–401 (2005) 268–278.
[2] D. Raabe, D. Ma, F. Roters, Acta Mater. 55 (2007) 4567–4583.
[3] D.E. Hurtado, M. Ortiz, J. Mech. Phys. Solids 60 (2012) 1432–1446.
[4] O. Kraft, P.A. Gruber, R. Mönig, D. Weygand, Annu. Rev. Mater. Res. 40 (2010) 293–317.
[5] C.A. Volkert, E.T. Lilleodden, Philos. Mag. Lett. 86 (2006) 5567–5579.
[6] C. Kiener, C. Motz, G. Dehm, Size effects in single crystal plasticity of copper under uniaxial loading, Dissertation, Publication C, IV, 2007, pp. 1–14.
[7] C. Kirchlechner, J. Keckes, C. Motz, W. Grosinger, M.W. Kapp, J.S. Micha, O. Ulrich, G. Dehm, Acta Mater. 59 (2011) 5618–5626.
[8] M.D. Uchic, P.A. Shade, D.M. Dimiduk, Annu. Rev. Mater. Res. 39 (2009) 361–386.
[9] C.P. Frick, B.G. Clark, S. Orso, A.S. Schneider, E. Arzt, Mater. Sci. Eng. A 489 (2008) 319–329.
[10] J.R. Greer, W.C. Oliver, W.D. Nix, Acta Mater. 53 (2005) 1821–1830.
[11] D.M. Dimiduk, M.D. Uchic, T.A. Parthasarathy, Acta Mater. 53 (2005) 4065–4077.
[12] D.M. Norfleet, D.M. Dimiduk, S.J. Polasik, M.D. Uchic, M.J. Mills, Acta Mater. 56 (2008) 2988–3001.
[13] D.M. Dimiduk, C. Woodward, R. Le Sar, M.D. Uchic, Science 312 (2006) 1188–1190.
[14] M. Zaiser, J. Schwerdtfeger, A.S. Schneider, C.P. Frick, B.G. Clark, P.A. Gruber, E. Arzt, Philos. Mag. 88 (2008) 3861–3874.
[15] K.S. Ng, A.H.W. Ngan, Philos. Mag. Lett. 87 (2007) 967–977.
[16] K.S. Ng, A.H.W. Ngan, Acta Mater. 56 (2008) 1712–1720.
[17] A. Kunz, S. Pathak, J.R. Greer, Acta Mater. 59 (2011) 4416–4424.
[18] N. Kheradmand, H. Vehoff, Adv. Eng. Mater. 14 (2012) 153–161.
[19] N. Kheradmand, H. Vehoff, A. Barnoush, Acta Mater. 61 (2013) 7454–7465.
[20] T. Hirouchi, Y. Shibutani, Mater. Trans. 55 (2014) 52–57.
[21] L.L. Li, X.H. An, P.J. Imrich, P. Zhang, Z.J. Zhang, G. Dehm, Z.F. Zhang, Scr. Mater. 69 (2013) 199–202.
[22] J.P. Hirth, Metall. Trans. 3 (1972) 3047–3067.
[23] K.T. Aust, N.K. Chen, Acta Metall. 2 (1954) 632–638.
[24] H. Vehoff, C. Laird, D.J. Duquette, Acta Metall. 35 (1987) 2877–2886.
[25] M.D. Sangid, T. Ezaz, H. Sehitoglu, I.M. Robertson, Acta Mater. 59 (2011) 283–296.
[26] T.C. Lee, I.M. Robertson, H.K. Birnbaum, Philos. Mag. A 62 (1) (1990) 131–153.
[27] Z. Shen, R.H. Wagoner, W.A.T. Clark, Acta Metall. 36 (1988) 3231–3242.
[28] W.M. Ashmawi, M.A. Zikry, Mech. Mater. 35 (2003) 537–552.
[29] L.C. Lim, R. Raj, J. Phys. Colloq. C4 (1985) 581–595.
[30] J. Gemperlová, V. Paidar, Czech. J. Phys. B 35 (1985) 351.
[31] J. Gemperlová, V. Paidar, F. Kroupa, Czech. J. Phys. B 39 (1989) 427–446.
[32] P. Peralta, C. Laird, Acta Mater. 45 (1997) 5129.
[33] P. Peralta, A. Schober, C. Laird, Mater. Sci. Eng. A 169 (1993) 43–51.
[34] T. Richeton, S. Berbenni, Eur. J. Mech. A/Solids 37 (2013) 231–247.
[35] C. Perrin, S. Berbenni, H. Vehoff, M. Berveiller, Acta Mater. 58 (2010) 4639–4649.

[36] H. Gleiter, The formation of annealing twins, Acta Metall. 17 (1969) 1421–1428.
[37] V. Randle, P.R. Rios, Y. Hu, Scr. Mater. 58 (2008) 130–133.
[38] C.S. Pande, M.A. Imam, B.B. Rath, Metal. Trans. 21A (1990) 2891–2896.
[39] Q. Li, J.R. Cahoon, N.L. Richards, Mater. Sci. Eng. A 527 (2009) 263–271.
[40] P. Neumann, in: Proceedings of the Seventh International Fatigue Congress, Beijing, 1999, pp. 107–113.
[41] T. Richeton, I. Tiba, S. Berbenni, in: Proceedings of the 13th International Symposium on Physics of Materials, Prague, 2014.
[42] C.A. Volkert, A.M. Minor, MRS Bull. 32 (2007) 389–399.
[43] W. Voigt, Lehrbuch Der Kristallphysik, B.G. Teubner, Leipzig, 1928.
[44] A. Acharya, J. Mech. Phys. Solids 49 (2001) 761–784.
[45] S. Berbenni, M. Berveiller, T. Richeton, Int. J. Solids Struct. 45 (2008) 4147–4172.
[46] A. Roy, R.H.J. Peerlings, M.G.D. Geers, Y. Kasyanyuk, Mater. Sci. Eng. A 486 (2008) 653–661.
[47] T.B. Britton, A.J. Wilkinson, Acta Mater. 60 (2012) 5773–5782.
[48] C. Rey, G. Saada, Philos. Mag. 33 (1976) 825–841.
[49] C. Rey, A. Zaoui, Acta Metall. 28 (1979) 687–697.
[50] T.L. Li, Y.F. Gao, H. Bei, E.P. George, J. Mech. Phys. Solids 59 (2011) 1147–1162.
[51] J.P. Hirth, J. Lothe, Theory of Dislocations, Wiley-Interscience, New York, 1982.